3D Tomographic Image Reconstruction for Multistatic Ground Penetrating Radar

Mauricio Pereira, Yu Zhang, Daniel Orfeo, Dylan Burns, Dryver Huston, Tian Xia

Abstract-Multistatic GPR has the advantages of reducing survey time and leverages more comprehensive data collection. Traditionally in multistatic GPR data processing, the 2D Bscan image obtained from each receive antenna are simply stacked for 3D image reconstructions. However, such approach is typically inadequate as the multistatic GPR receivers are mounted with spatial offsets, causing back-scattering signals from the same target to have differing time of arrivals. For proper fusion of multistatic GPR data, migration methods that consider the transmitters and receivers spatial offset and data variations among different receiving antennas may be employed. In this study, the back-projection algorithm (BPA) is investigated. The algorithm consists of determining the wave travel path and associated travel time, and projecting the corresponding signal value back into space domain. Furthermore, antenna radiation pattern is incorporated. The BPA enables scatter shape reconstruction and is prone to parallel computing. For validation, multistatic GPR 3D tomographic image reconstruction is successfully applied to laboratory data.

Keyword: Multistatic GPR, 3D imaging, tomography

I. INTRODUCTION

Ground penetrating radar (GPR) is a subsurface sensing method that consists in emitting an electromagnetic pulse into the ground and sensing the scattered electromagnetic wave[1], [2]. It has been applied in the survey and mapping of buried pipes [3], landmine detection [4], assessment of bridge decks [5], [6], rebar detection [7], pipe leak detection [8], soil characterization [9], concrete and railroad defect characterization [10], [11], through-wall sensing [12], and recently to vehicle localization [13]. Comercially available GPR systems usually rely on wheel encoders and a typical GPR survey is performed by scanning along multiple parallel lines. Each linear scan forms a 2D image denominated Bscan. The columns of a B-scan corresponds to range profile waveforms referred as A-scans. To form 3D images of the subsurface, parallel B-scans are stacked forming a C-scan. A multistatic GPR system in which several receiver antennas are arranged alongside, for instance, can reduce survey time by covering a larger area in a single pass.

In multistatic GPR data processing, the construction of 3D images by simple stacking of 2D B-scans, however, is inadequate because the same buried feature will be perceived at different depths due to the phase shift caused by the change of GPR system position or spatial offset of different receive antennas. Moreover, averaging all receive antennas signal

without phase compensation can not guarantee to improve signal-to-noise ratio (SNR).

Therefore, to properly fuse multistatic GPR data, a migration algorithm that considers the relative positions of transmitters and receivers is required. Also, for air-coupled GPR survey [14], [15], a migration algorithm that incorporates the air layer in its migrating process is desirable. A host of migration algorithms have been employed in GPR data processing, such as Kirchhoff's migration [16], Stolt migration [17], phase shift migration [18], synthetic aperture radar (SAR) migration [19], back-projection algorithm (BPA) [20], [21], etc.

For 2D image formation, [22] shows that the Stolt migration and BPA achieve good signal focusing, with the Stolt migration being slightly faster to compute. However, the BPA can easily incorporate layered media, such that both ground-coupled and air-coupled GPR data can be processed. The BPA consists in determining the wave travel path, and the associated travel time, from transmitter to receiver and then back-projecting the corresponding signal into the space domain. This process is performed for every A-scan collected, and the back-projected signals are added to the same space domain. Strong scattering points in the space domain considered will receive contributions from several Ascans increasing SNR, as illustrated in Fig. 1. If the scattering target is volumetric, this process is able to recover the buried feature shape by constructive interference of the backprojected waves. The main contribution of this paper is the formulation, implementation and validation, of a 3D imaging algorithm for both ground and air-coupled multistatic GPR.

This paper is organized as follows: in the methodology section, the 2D BPA for a bistatic GPR system is presented and then extended to 3D bistatic GPR, and finally to 3D multistatic GPR. In the results section, the laboratory multistatic GPR system is described, and the BPA reconstructed images are presented and discussed. In the conclusions, the final remarks and future directions are discussed.

II. METHODOLOGY

To apply the BPA, it is necessary to determine the wave travel path and calculate the wave travel time, such that the receiving signal can be back-projected to the scatterer. In the next section, the 2D geometry of both ground-coupled and air-coupled bistatic GPRs are considered as the prototypes for developing 3D multistatic GPR presented in subsequent sections.

^{*}This work is supported by the NSF Grants No. 1647095 and No. 1640687, the UVM SparkVT Fund, and VT EPSCoR

¹School of Engineering, University of Vermont, Burlington, VT 05405, USA

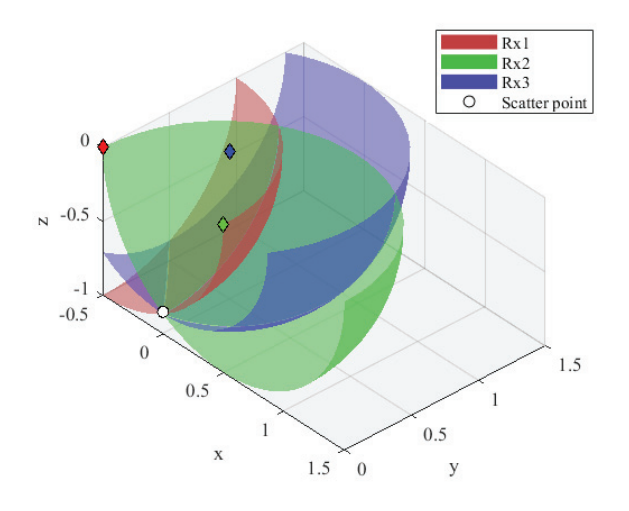


Fig. 1. The traces of three different receivers are back-projected into space domain. The scattering point gets reinforced by all the traces.

A. 2D bistatic GPR geometry

Consider the ground-coupled bistatic GPR in Fig. 2. The transmitter antenna and receiver antenna have a spatial offset ΔL . They move in the indicated direction in N discrete steps. At the k^{th} step, the transmitter and receiver are at positions $P_T^{[k]}$ and $P_R^{[k]}$, respectively. Let $d_{AB}^{[k]} = \|B - A\|_2$ denote the Euclidean distance between two points A and B at the k^{th} step position. Given a feature point P and the subsurface dielectric constant ε , the wave path can be calculated as

$$d^{[k]} = d_{P_T P}^{[k]} + d_{P P_R}^{[k]} \tag{1}$$

and the associated wave travel time as

$$t_P^{[k]} = d^{[k]}/v,$$
 (2)

where $v = c/\sqrt{\varepsilon}$ and c is the speed of light.

Let the A-scan trace received at position k be $s^{[k]}(t)$. In BPA algorithm, each A-scan data $s^{[k]}(t_p)$ can be back projected to a scattering point that is t_p away from the receiver. However as there are multiple points that are of the same distance from the receiver, $s_p^{[k]}$ will be back-projected into a curve over the space domain. When BPA is applied to all A-scan traces, different curves will intersect at a common point which specifies the true scatterer.

For the air-coupled bistatic GPR shown in Fig. 3, the main difference in relation to the ground-coupled GPR is that the ground scattering point position x_S must be determined for the calculation of the wave travel path and time in both air and ground. For that purpose, an approximation given by [21] is applied:

$$x_{S}(P, P_{T}^{[k]}) = \begin{cases} x_{P} + \frac{x_{C} - x_{P}}{\sqrt{\varepsilon}}, & \text{if } |x_{T} - x_{P}| < d_{cr} \\ x_{P} + \frac{z_{P}}{\sqrt{\varepsilon} - 1}, & \text{if } x_{T} \ge x_{P} + d_{cr} \\ x_{P} - \frac{z_{P}}{\sqrt{\varepsilon} - 1}, & \text{if } x_{T} \le x_{P} - d_{cr} \end{cases}$$
(3)

where $P=(x_P,z_P)$ is a subsurface point of interest, $P_T^{[k]}=(x_T,-h)$ and $P_R^{[k]}=(x_R,-h)$ are the transmitter and receiver positions. $d_{cr}=(z_P+h)\sqrt{\frac{\varepsilon}{(\varepsilon-1)}}, h$ is the mounting height of antennas. Equation (3) gives the scattering point P_S between the transmitter at $P_T^{[k]}$ and P. The same equation can be used to calculate the scattering point P_S^* between P and the receiver at position $P_R^{[k]}$ as $x_S(P,P_R^{[k]})$ since the geometry is symmetric. The point $P_C=(x_C,0)$ is the intersection between the ground level and a line connecting the transmitter to the point P. An analogous point P_C^* can be determined connecting P and the receiver. The wave travel path is then given by

$$d^{[k]} = d_{P_T P_S}^{[k]} + d_{P_S P}^{[k]} + d_{P_P S}^{[k]} + d_{P_S^* P_R}^{[k]}$$

$$\tag{4}$$

and the travel time as

$$t_P^{[k]} = (d_{P_T P_S}^{[k]} + d_{P_T^* P_P}^{[k]})/c + (d_{P_S P}^{[k]} + d_{PP_T^*}^{[k]})/v. \tag{5}$$

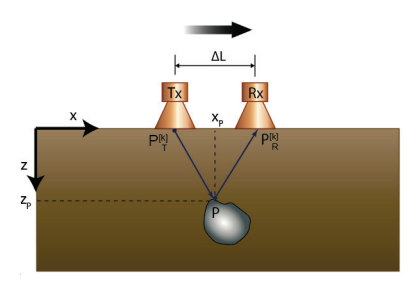


Fig. 2. Schematic of a 2D bistatic ground-coupled GPR [23].

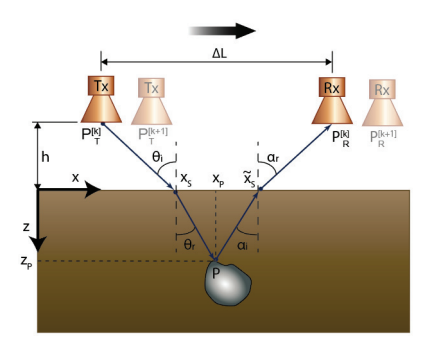


Fig. 3. Schematic of a 2D bistatic air-coupled GPR [23].

B. 3D bistatic GPR geometry

The ground-coupled case can be readily extended to the 3D back-projection by adding an extra dimension to the domain of interest, where equations (1) and (2) still apply. For the air-coupled case, consider the transmitter and receiver shown in Fig. 4 at arbitrary positions $P_T^{[k]}$ and $P_R^{[k]}$, respectively. Define a local frame of reference O'x'y'z' that is attached to the transmitter, but at ground level, whose x' axis points to the receiver direction. As shown in Fig. 5, this local frame of reference forms an angle ϕ with a fixed global frame of reference Oxyz. Then it is possible to apply the approximation given by Eq. (3) in the x'-z' plane, and perform a homogeneous transformation \mathbf{H} to express

it in terms of the Oxyz coordinates. The homogeneous transformation is expressed as $\mathbf{v} = \mathbf{H}\mathbf{v}'$ [24] where

$$\mathbf{H} = \begin{bmatrix} \cos(\phi) & -\sin(\phi) & 0 & x_T \\ \sin(\phi) & \cos(\phi) & 0 & y_T \\ 0 & 0 & 1 & 0 \\ 0 & 0 & 0 & 1 \end{bmatrix}, \tag{6}$$

corresponding to a translation of the origin $O' = (x_T, y_T, 0)$ and a rotation of ϕ degrees about the z = z' axis, $\mathbf{v} = (x, y, z, 1)^T$ and $\mathbf{v}' = (x', y', z, 1)^T$ are the homogeneous coordinates in the global and local reference systems, respectively. For a point of interest $P = (x_P, y_P, z_P)$ and a transmitter position $P_T = (x_T, y_T, -h)$, the resulting approximation of the ground scattering point $P_S = (x_S, y_S, 0)$ can be calculated as

$$x_{S} = \begin{cases} x_{P} + \frac{z_{P}(x_{T} - x_{P})}{\sqrt{\varepsilon}(z_{P} + h)}, & \text{if } |x_{P} - x_{T}| \leq |cos(\phi)|d_{cr} \\ x_{P} - \frac{z_{P}cos(\phi)}{\sqrt{\varepsilon - 1}}, & \text{if } |x_{P} - x_{T}| > |cos(\phi)|d_{cr} \end{cases},$$
(7)

$$y_S = y_T + \frac{y_P - y_T}{x_P - x_T} (x_S - x_T),$$
 (8)

with

$$cos(\phi) = \frac{x_P - x_T}{\sqrt{(x_P - x_T)^2 + (y_P - y_T)^2}}.$$
 (9)

With equation (7), it is now possible to apply equations (4) and (5) for the 3D air-coupled case.

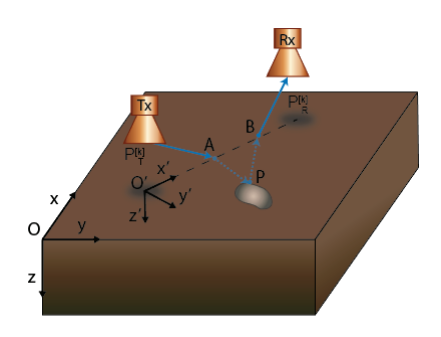


Fig. 4. Schematic of a 3D bistatic air-coupled GPR [23].

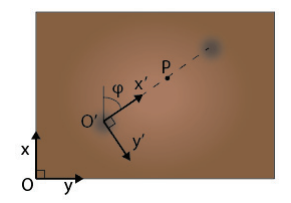


Fig. 5. Topview schematic of a 3D bistatic air-coupled GPR [23].

C. 3D BPA for bistatic GPR

To implement the BPA, a set of M points of interest in the subsurface domain are selected. Suppose that a bistatic GPR scan produces N A-scan traces at different positions. For each position k = 1...N, the travel time $t_{i,k}$ to an underground scattering point P_i , i = 1...M, can be calculated using (2) for ground-coupled GPR scan or (5) for air-coupled GPR scan.

Furthermore, consider that the receiver antenna has a directivity with a gain function $g(\theta_{i,k})$ where $\theta_{i,k}$ is the angle formed between the z axis and a line connecting the receiver at $P_R^{[k]}$ to a point P_i . Then the signal value back projected at point P_i is $\hat{s}_{i,k} = g(\theta_{i,k})s_{i,k}$, where $s_{i,k} = s^{[k]}(t_{i,k})$ is the unattenuated received signal at position k. Let the addition of $\hat{s}_{i,k}$ to the point P_i be denoted as $\hat{s}_{i,k}|_{P_i}$. Then the BPA image is formed with the superposition of $\hat{s}_{i,k}$ at all points P_i , i = 1...M for all positions k = 1...N,

$$\mathscr{I} = \sum_{k=1}^{N} \sum_{i=1}^{N} \hat{s}_{i,k}|_{P_i} = \sum_{k=1}^{N} \sum_{i=1}^{N} g(\theta_{i,k}) s_{i,k}|_{P_i}$$
(10)

D. 3D BPA for multistatic GPR

Assume a multistatic GPR system is composed of Q transmitters and R receivers. For the scan initialized by the q^{th} transmitter at position k, the A-scan signal received by the r^{th} receiver is $s^{[q,r,k]}(t)$. This signal value at the travel time to the point P_i is denoted $s^{q,r}_{i,k} = s^{[q,r,k]}(t^{[k]}_{P_i})$. Applying the antenna directivity we have $s^{q,r}_{i,k} = g(\theta_{i,k})s^{q,r}_{i,k}$. Thus Eq. (10) can be applied for image formation for the set of A-scan traces obtained between each specific transmitter r and receiver q pair

$$\mathscr{J}^{q,r} = \sum_{k=1}^{N} \sum_{i=1}^{N} \hat{s}_{i,k}^{q,r} | P_i, q = 1...Q, r = 1...R.$$
 (11)

The multistatic GPR BPA image is then formed by adding all sub-images $\mathscr{I}^{q,r}$

$$\mathscr{I} = \sum_{q=1}^{Q} \sum_{r=1}^{R} \mathscr{I}^{q,r}.$$
 (12)

III. RESULTS

For the set of points P_i in a regular grid, the image can be formed using a 3D matrix to store the composed values.

To enhance the image quality, normalization is performed by the highest BPA image absolute value $\|\mathscr{I}\|_{\infty} = \max_{i,j,k} |\mathscr{I}|$, where i,j,k are the 3D matrix indices, such that

$$\mathscr{I}_{norm} = \frac{\mathscr{I}}{\|\mathscr{I}\|_{\infty}}.$$
 (13)

As introduced in the preceding section, an additional advantage of BPA is that it is suitable for parallel computing. In this study, the parallel computing program CUDA API is adopted, which facilitates to leverage the data processing speed.

A. Multistatic GPR system

In the experimental study, a multistatic GPR system composed of one transmitter and three receiver antennas is employed. The system is controlled by a 4-channel Keysight PNA-X Network Analyzer. The antennas have been projected and manufactured in our laboratory. Its bandwidth spans from 700 MHz to 6 GHz [25]. The antenna pattern is shown in Fig. 6. The sand dielectric constant is $\varepsilon = 3$.

The antennas are at a height of 0.3 m from the ground, and their arrangement is shown in Fig. 7.

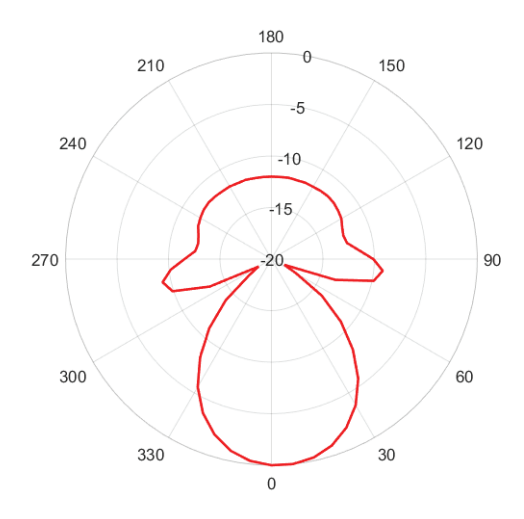


Fig. 6. Antenna pattern

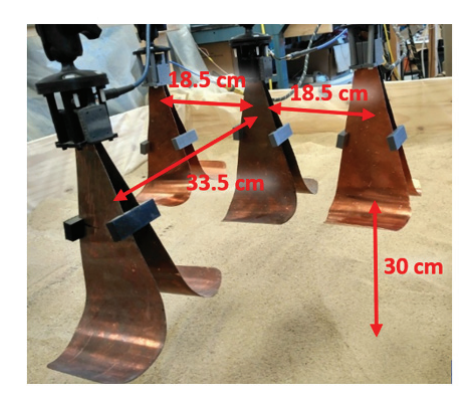


Fig. 7. Multistatic GPR configuration. The first antenna is a transmitter antenna and other three are receiver antennas. The system is controlled by a Keysight PNA-X Network Analyzer (not shown in the picture).

Each experiment data set is composed of 15 parallel B-scans whose transversal step size is 25.4 mm, as shown in Fig. 8. Each B-scan is composed of 90 A-scan traces whose longitudinal step size is 10 mm.

B. 3D BPA images

- 1) Ground level complex shape: A metal object of complex shape shown in Fig. 9 is placed at the ground level. For the image reconstruction, a regular grid of $80 \times 80 \times 30$ points is created over a domain size of $0.3 \times 0.6 \times 0.15$ (m). The cross-section on the x-y plane, parallel to the ground, is show in Fig. 10. An isosurface at +0.35 of the resulting 3D image is presented in Fig. 11, the object shape is recovered with good accuracy.
- 2) Buried metal plate: A metal plate target shown in Fig. 12 is buried at a depth of about 75 mm. For the image reconstruction, a regular grid of $60 \times 60 \times 40$ points is used over a domain size of $0.4 \times 0.4 \times 0.15$ (m). The cross-sections of the resulting BPA image are shown in Fig. 13. Reconstruction on the x-z plane has a finer resolution as more data are collected in that direction, but a reasonably good reconstruction is also observed in the x-y plane. An isosurface at -0.4 of the resulting 3D image is presented

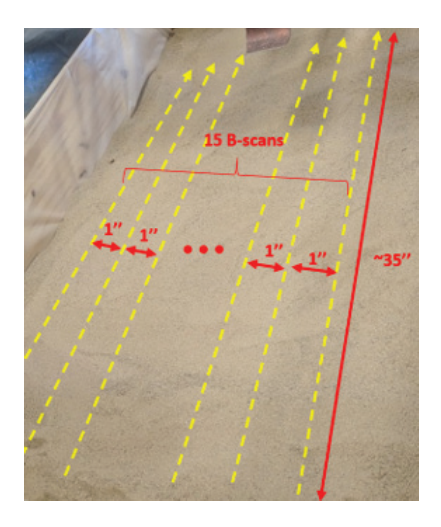


Fig. 8. Sandbox scan profile.



Fig. 9. Copper complex shape surface target.

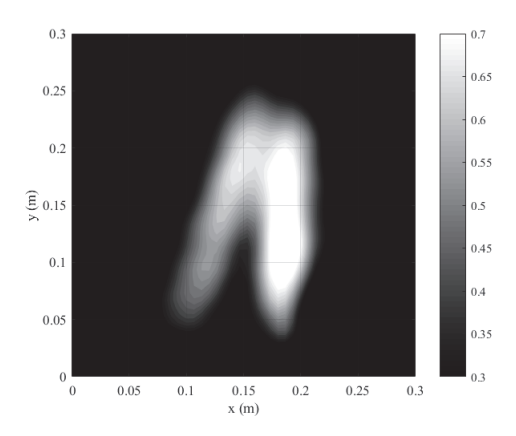


Fig. 10. Slice in the x-y plane of the reconstructed image.

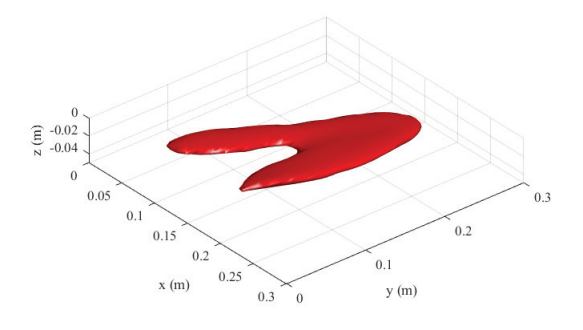


Fig. 11. Isosurface at +0.35 of the BPA image showing the recovery of a complex shape of a target at ground level.

in Fig. 14. Since the final image is simply normalized as per equation (13), negative values correspond to polarity inversion of the scattered signal. The value was selected by image inspection. As can be observed, the object shape is also recovered with a good fidelity.



Fig. 12. Aluminum plate used as a buried target.

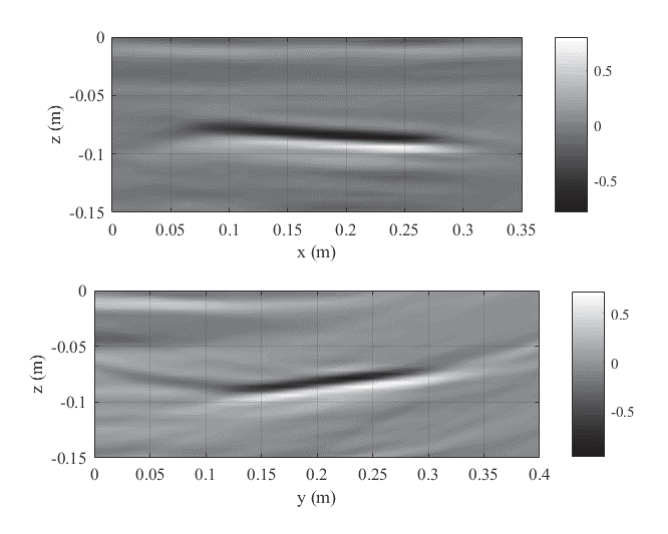


Fig. 13. Cross-sections of the 3D BPA image of a metal plate buried at 50 mm depth.

3) Buried metal disk: A metal disk target shown in Fig. 15 is buried at a depth of about 75 mm. For the image reconstruction, a regular grid of $60 \times 60 \times 40$ points was used over a domain size of $0.4 \times 0.4 \times 0.15$ (m). The cross-sections of the resulting BPA image are shown in Fig. 13. An

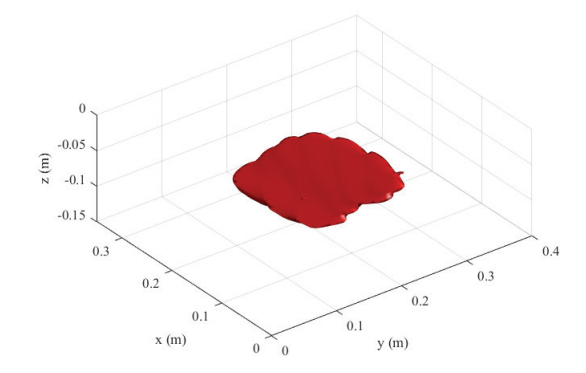


Fig. 14. Isosurface at -0.4 showing the recovery of the rectangular shape of a buried metal plate.

isosurface at -0.35 of the resulting 3D image is presented in Fig. 14, also with a good fidelity.



Fig. 15. Metal disk used as a buried target.

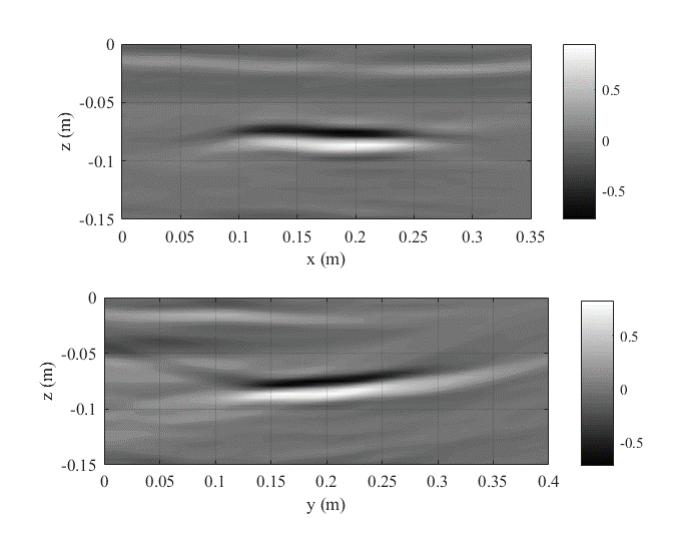


Fig. 16. Cross-sections of the 3D BPA image of a metal disk buried at $50 \, \mathrm{mm}$ depth.

IV. CONCLUSIONS

In this paper, a fast 3D BPA algorithm is investigated and successfully applied for multistatic GPR image construction for two buried targets, and a complex shape at ground level. A multistatic GPR system, consisting of one transmitter and three receivers, and controlled by a Keysight PNA-X network analyzer is used to collect the GPR A-scan traces. The antenna radiation pattern is considered in the

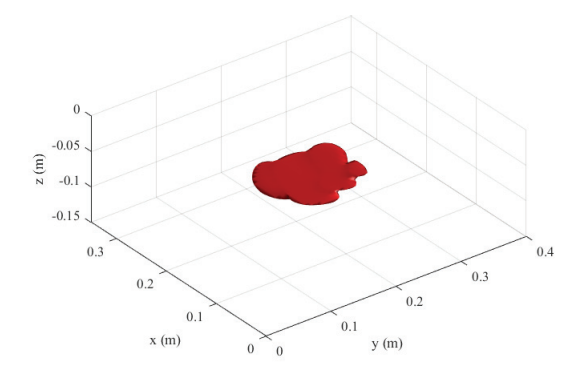


Fig. 17. Isosurface at -0.35 showing the recovery of a buried metal disk.

back-projection process, aiding in the reduction of BPA artifacts. Furthermore, to reduce computational complexity, an approximation of the scattering point for air-coupled GPR is applied. Future research includes the extension of the back-projection algorithm to distributed sensing systems and comparison to other 3D imaging algorithms.

REFERENCES

- [1] J. D. Daniels, *Ground Penetrating Radar*, 2nd ed. London, UK: The Institution of Electrical Engineers, 2004.
- [2] H. M. Jol, Ground penetrating radar: theory and applications, 1st ed. Amsterdam, Netherlands: Elsevier Science, 2009.
- [3] D. Huston, T. Xia, Y. Zhang, T. Fan, D. Orfeo, and J. Razinger, "Urban underground infrastructure mapping and assessment," no. April, 2017.
- [4] X. Feng and M. Sato, "Pre-stack migration applied to GPR for landmine detection," *Inverse Problems*, vol. 20, no. 6, 2004.
- [5] A. M. Alani, M. Aboutalebi, and G. Kilic, "Applications of ground penetrating radar (GPR) in bridge deck monitoring and assessment," *Journal of Applied Geophysics*, vol. 97, pp. 45–54, 2013. [Online]. Available: http://dx.doi.org/10.1016/j.jappgeo.2013.04.009
- [6] Z. W. Wang, M. Zhou, G. G. Slabaugh, J. Zhai, and T. Fang, "Automatic Detection of Bridge Deck Condition from Ground Penetrating Radar Images," *IEEE Transactions on Automation Science & Engineering*, vol. 8, no. 3, pp. 633–640, 2011.
- [7] Y. Zhang, A. S. Venkatachalam, D. Huston, and T. Xia, "Advanced signal processing method for ground penetrating radar feature detection and enhancement," in *Proceedings of SPIE Smart Structure and NDE Conference*, vol. 9063, 2014, p. 906318.
- [8] S. Demirci, E. Yigit, I. H. Eskidemir, and C. Ozdemir, "Ground penetrating radar imaging of water leaks from buried pipes based on back-projection method," NDT and E International, vol. 47, pp. 35–42, 2012. [Online]. Available: http://dx.doi.org/10.1016/j.ndteint.2011.12.008
- [9] Y. Zhang, D. Burns, D. Huston, and T. Xia, "Sand moisture assessment using instantaneous phase information in ground penetrating radar data," in *Proceedings of SPIE Smart Sturcture and NDE Conference*, vol. 9437, 2015, p. 943726.
- [10] Q. Ye, L. Jiao, C. Liu, D. Huston, and T. Xia, "Extracting and identifying concrete structural defects in GPR imagesw," in *Proceedings of SPIE Vol 10599*, 2018.
- [11] Y. Zhang, A. S. Venkatachalam, and T. Xia, "Ground-penetrating radar railroad ballast inspection with an unsupervised algorithm to boost the region of interest detection efficiency," *Journal of Applied Remote Sensing*, vol. 9, no. 1, p. 095058, 2015.
- [12] Y. Zhang and T. Xia, "In-wall clutter suppression based on low-rank and sparse representation for through-the-wall radar," *IEEE Geoscience and Remote Sensing Letters*, vol. 13, no. 5, pp. 671–675, 2016.
- [13] M. Cornick, J. Koechling, B. Stanley, and B. Zhang, "Localizing ground penetrating radar: A step toward robust autonomous ground vehicle localization," *Journal of Field Robotics*, vol. 33, no. 1, pp. 82–102.

- [14] I. Al-Qadi, W. Xie, R. Roberts, and Z. Leng, "Data Analysis Techniques for GPR Used for Assessing Railroad Ballast in High Radio-Frequency Environment," *Journal of Transportation Engineering*, vol. 136, no. 4, pp. 392–399, 2010.
- [15] X. Xu, T. Xia, A. Venkatachalam, and D. Huston, "Development of High-Speed Ultrawideband Ground-Penetrating Radar for Rebar Detection," *Journal of Engineering Mechanics*, vol. 139, no. 3, pp. 272–285, 2013.
- [16] W. A. Schneider, "Integral Formulation for Migration in Two and Three Dimensions," *Geophysics*, vol. 43, no. 1, pp. 49–76, 1978.
- [17] R. H. Stolt, "Migration By Fourier Transform," Geophysics, vol. 43, no. 1, pp. 23–48, 1978.
- [18] J. Gazdag, "Wave equation migration with the phaseshift method," Geophysics, vol. 43, no. 7, pp. 1342–1351, 1978. [Online]. Available: http://library.seg.org/doi/10.1190/1.1440899
- [19] J. I. Halman, K. A. Shubert, and G. T. Ruck, "SAR processing of ground-penetrating radar data for buried UXO detection: results from a surface-based system," *IEEE Transactions on Antennas and Propagation*, vol. 46, no. 7, pp. 1023–1027, 1998.
- [20] J. E. Mast and E. M. Johansson, Three-dimensional groundpenetrating radar imaging using multifrequency diffraction tomography, sep 1994, vol. 2275.
- [21] L. Zhou, C. Huang, and Y. Su, "A fast back-projection algorithm based on cross correlation for GPR imaging," *IEEE Geoscience and Remote Sensing Letters*, vol. 9, no. 2, pp. 228–232, 2012.
- [22] C. Ozdemir, S. Demirci, E. Yigit, and B. Yilmaz, "A review on migration methods in b-scan ground penetrating radar imaging," *Mathematical Problems in Engineering*, vol. 2014, 2014.
- [23] M. Pereira, Y. Zhang, D. Orfeo, D. Burns, D. Huston, and T. Xia, "3D tomography for multistatic GPR subsurface sensing," in *Proceedings of SPIE Vol* 10633, 2018.
- [24] A. A. Shabana, Dynamics of multibody systems, 1st ed. US: John Wiley & Sons, 1989.
- 25] A. Ahmed, Y. Zhang, D. Burns, D. Huston, and T. Xia, "Design of uwb antenna for air-coupled impulse ground-penetrating radar," *IEEE Geoscience and Remote Sensing Letters*, vol. 13, no. 1, pp. 92–96, 2016